

Dynamic Observation of Retinal Response to Pressure Elevation in a Microfluidic Chamber

Alberto Esteban-Linares, Lauren K. Wareham,* Thayer S. Walmsley, Joseph M. Holden, Matthew L. Fitzgerald, Zhiliang Pan, Ya-Qiong Xu, and Deyu Li*



Cite This: *Anal. Chem.* 2022, 94, 12297–12304



Read Online

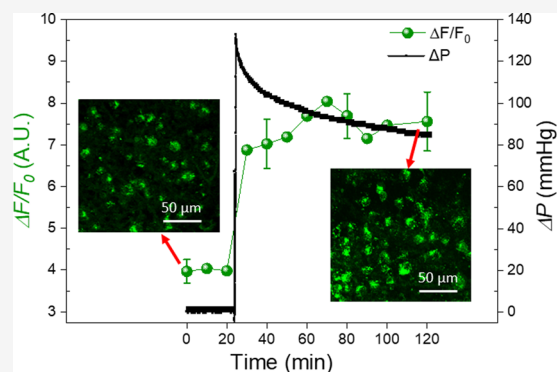
ACCESS |

Metrics & More

Article Recommendations

Supporting Information

ABSTRACT: Dynamic observation of cell and tissue responses to elevated pressure could help our understanding of important physiological and pathological processes related to pressure-induced injury. Here, we report on a microfluidic platform capable of maintaining a wide range of stable operating pressures (30 to 200 mmHg) while using a low flowrate (2–14 $\mu\text{L}/\text{h}$) to limit shear stress. This is achieved by forcing flow through a porous resistance matrix composed of agarose gel downstream of a microfluidic chamber. The flow characteristics were investigated and the permeabilities of the agarose with four different concentrations were extracted, agreeing well with results found in the literature. To demonstrate the capability of the device, we measured the change in intracellular Ca^{2+} levels of retinal ganglion cells in whole mouse retina in response to pressure. The onset of enhanced pressure results in, on average, an immediate 119.16% increase in the intracellular Ca^{2+} levels of retinal ganglion cells. The demonstrated microfluidic platform could be widely used to probe cell and tissue responses to elevated pressure.



Biological responses to pressure have been widely reported in cells and tissues.^{1–3} In diseases where changing pressures can directly influence the survival of tissues, understanding the pathological cellular mechanisms becomes critical. In the eye, an internal pressure is constantly maintained (intraocular pressure; IOP) and is important for the ocular structure and stability. IOP naturally exhibits diurnal fluctuations; however, acute or extreme elevations in IOP can occur as a result of traumatic ocular or brain injury,^{4–7} and persistent increases in IOP with the development of progressive eye diseases such as glaucoma can lead to irreversible blindness.⁸ Understanding how and why retinal ganglion cells (RGCs) and other retinal cells respond to changes in pressure is vital in our development of future therapeutics for glaucoma and ocular trauma.

In many cell types including neurons, Ca^{2+} signaling is critical for maintaining proper neuronal function,^{9,10} and fluctuations in the intracellular concentration of Ca^{2+} can control many cellular and physiological processes, including neurotransmitter release, hormone secretion, and gene expression.^{9,11} Ca^{2+} signaling is routinely measured using fluorescently labeled Ca^{2+} -sensitive reporters, such as Fluo-4 AM.^{12,13} In the retina, the function and viability of RGCs is reduced in part by perturbed intracellular Ca^{2+} signaling.⁹ Pressure-induced increases in intracellular Ca^{2+} have been linked with apoptosis of multiple retinal cells.^{12,14,15} However, these studies are hampered by the inability to detect dynamic Ca^{2+} changes with pressure. Previous studies have been

performed in vitro in pressurized incubators (reaching pressures exceeding 70 mmHg) with observation of cell behaviors after cells and tissues have been moved to ambient conditions.^{16,17} This prevents observation of cellular responses at shorter time intervals, potentially obscuring studies of more immediate cell responses, including Ca^{2+} changes, to pressure. So far, most reports on the effect of elevated pressure on retinal cells have been carried out in vivo or in vitro, with very few ex vivo studies. However, ex vivo assays could provide valuable information on the mechanism, morphology, intracellular complexity, and neuronal connections of the retina. Furthermore, ex vivo studies provide additional advantages as they are rapid, cost-effective, and generally easier to implement.¹⁸ While some progress has been made utilizing ex vivo experiments to observe the effect of elevated pressure on rat retinal tissue, the pressure and corresponding cell responses are not monitored dynamically.^{19,20}

Two techniques are commonly used to achieve elevated pressures in a microfluidic chamber: forcing flow through a porous matrix or using a hydrostatic pressure approach. For

Received: December 31, 2021

Accepted: August 15, 2022

Published: August 26, 2022



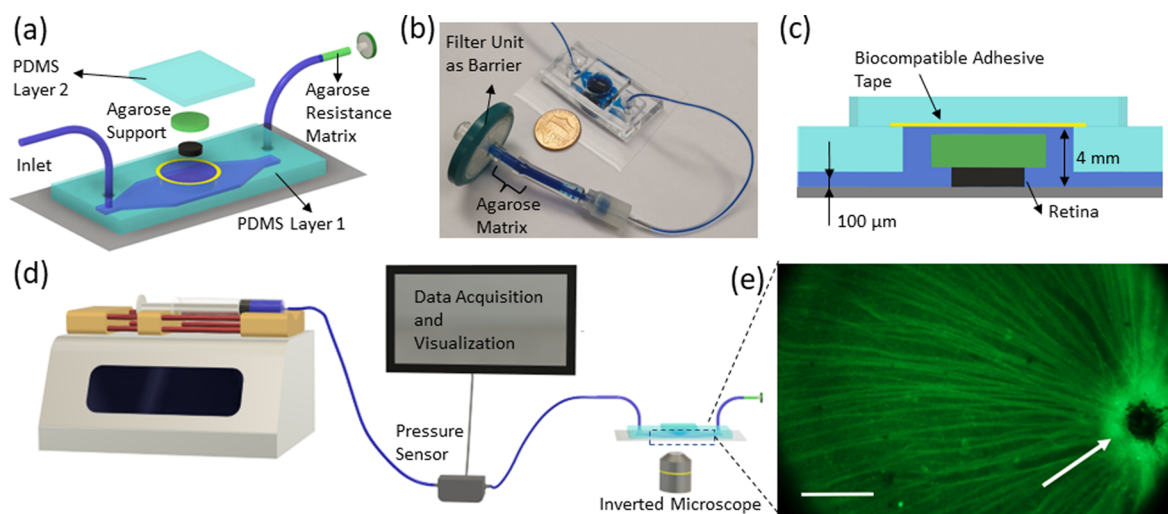


Figure 1. (a) Exploded view of the device showing PDMS (light blue), media (dark blue), glass coverslip (light gray), biocompatible adhesive tape (yellow), explanted retina (black), agarose gel (green) used to adhere retina to the coverslip, and agarose porous matrix to increase the pressure drop. Figure not drawn to scale. (b) Picture of the final assembled device filled with blue color dye. Agarose resistance matrix is pushed against the filter unit at the outlet. (c) Cross-section schematic of the assembled microfluidic platform where the retina is flattened and securely fixed on the glass coverslip. Figure not drawn to scale. (d) Schematic of the experimental setup used to measure the pressure inside the microfluidic platform with the agarose resistance matrix and to monitor dynamic changes in RGCs Ca^{2+} intracellular markers. (e) Large field fluorescence image of green CTB-labeled retina flat-mounted in device (arrow indicates optic nerve head). Scale bar is $200\ \mu\text{m}$.

the hydrostatic approach, pressure is governed by Pascal's law; and to achieve a pressure of 70 mmHg, a fluid height of ~ 75 cm is needed, which renders the experiment not feasible under a microscope. As such, forcing flow through a porous matrix is more compatible with dynamic observation of cell/tissue response to pressure.²¹ Flow through micro/nanoporous materials is important for a wide range of applications,^{22,23} and efforts to understand flow through porous media have been carried out for microchannels filled with randomly aligned packed-bed of solid spheres,²⁴ two-dimensional array of posts,²⁵ or polymer monoliths.²⁶ Channels filled with posts or solid spheres are convenient approaches;²⁷ however, it is difficult to achieve pressures over 70 mmHg as the flowrate needed is on the order of hundreds of $\mu\text{L}/\text{min}$, which could induce high shear stress that is not ideal for bioassays. Microchannels filled with porous polymer monoliths have been used mainly for chromatography applications and flow characteristics have been studied with varying fabrication parameters.²⁸ Even though it is possible to reach high pressure levels while maintaining polymer structural integrity, flowrates larger than $100\ \mu\text{L}/\text{h}$ are needed to reach our targeted pressures, which could still impose undesirable shear stress on the sample.

In this study, we report on a microfluidic platform capable of generating a wide range of chamber pressures (30 to 200 mmHg) while using a low flowrate ($2\text{--}14\ \mu\text{L}/\text{h}$) to minimize shear stress. The pressure change is induced by forcing flow through an agarose porous matrix, a biocompatible polysaccharide gel consisting of a large number of interconnected fibers with microscopic pores. As a proof of concept, we utilize whole mouse retina to demonstrate that the device enables *ex vivo* imaging of RGC intracellular Ca^{2+} fluorescence in direct response to elevated pressure. Results show that the RGC intracellular Ca^{2+} level increases immediately (+119.16%) in response to an elevated pressure of ~ 80 mmHg. Furthermore, we show that after cells are exposed to elevated pressure, decreasing pressure to baseline does not result in an immediate

decrease in intracellular Ca^{2+} fluorescence. This microfluidic platform could be readily utilized in the study of a wide range of mechanosensitive tissues and their responses to pressure.

EXPERIMENTAL SECTION

Device Design and Assembly. The microfluidic pressure chamber has three main components besides the glass coverslip substrate: PDMS Layer 1 composed of a microfluidic chamber and connecting channels for tissue placement and culture, PDMS Layer 2 with adhesive tapes to seal the chamber, and tygon tubing with an agarose matrix encapsulated as a resistance matrix (Figure 1a). It should be noted that PDMS Layer 2 and the agarose-filled tubing are assembled after an explanted retina is placed in the device, which allows for tissue culture under normal pressure and then observation of tissue in response to elevated pressures. Figure 1b shows a picture of the fully assembled device filled with blue food dye for visualization.

PDMS Layer 1 holds the microfluidic chamber for retina placement. This layer is fabricated by conventional soft-lithography techniques using a SU-8 mold, as described in the Supporting Information. The design is composed of a single fluidic pathway with three sections. The up- and down-stream sections are the inlet and outlet channels, respectively, which are 3 mm wide, 4 mm long, and $100\ \mu\text{m}$ tall. These two channels connect to a rectangular chamber of 8×11 mm through a diverging and converging triangular channel section, respectively. The middle section is manually punched through to create an open chamber of 8 mm in diameter and 4 mm tall, where the retina is placed once explanted. The thickness of the retina is $\sim 180\ \mu\text{m}$ in mice,²⁹ and the agarose support is ~ 1.5 mm thick. PDMS Layer 1 is then bonded to a No. 1 glass coverslip ($130\ \mu\text{m}$ thick) via O_2 plasma treatment. Figure 1c shows a schematic of the cross-section of the assembled microfluidic platform where the up- and down-stream channels and the 4 mm tall retina well are shown.

PDMS layer 2 is used to irreversibly seal the pressure chamber once retina is placed in the device. Achieving a rapid, biocompatible, and irreversible bonding of these two layers that can withstand an elevated pressure is crucial for the overall performance of the device. Air or oxygen plasma bonding is the most conventional technique to irreversibly bond PDMS to PDMS. However, this is not feasible for our device as we cannot expose PDMS layer 1 with retina in place to oxygen/air plasma. Other well-known bonding techniques, such as curing or partially curing of PDMS, were not suitable here either because these bonding methods either require a long period of curing at room temperature or need elevated temperature (60–80 °C) that is not compatible with retinal culture. Pressure-sensitive biomedical adhesive tapes provide a viable, rapid, and reliable approach in assembling microfluidic components. Importantly, previous work showed that the tapes did not degrade nor lose functionality even after seven days of incubation.³⁰ Furthermore, we compared the bonding strength to assess the quality of this bonding to a reference oxygen plasma treatment 30 min prior to the bonding (this time delay is due to the transfer of the device from where the oxygen plasma tool is to the confocal microscope room and the time needed for retina placement) and two other potential bonding techniques for the assembly of the device, where pressure-sensitive tapes exhibited the best performance (Figure S1). Therefore, biocompatible adhesive tape ARcare 92712 (Adhesive Research, UK) was chosen as the bonding approach in this work because of its high burst pressure and easy implementation.

Tygon tubing containing the agarose gel is attached to the outlet section of the device through a fitter. To prepare the agarose matrix, high gelling powder agarose (Sigma Aldrich, Saint Louis, MO) at different concentrations was dissolved in DI water at 120 °C. Once agitated and dissolved, the liquid mixture was forced into a Tygon ND-100-65 tube (Saint-Gobain Performance Plastics, Courbevoie, France) with an inner diameter of 2.38 mm and pushed against a 0.22 μm filter unit (Sigma Aldrich, St. Louis, MO) to avoid slippage (Figure 1a). Lastly, agarose gel is solidified by gelling at room temperature for 30 min.

Figure 1d depicts the experimental setup to measure the pressure drop in a microfluidic chamber. The microfluidic chamber was connected to a syringe pump (Harvard Apparatus, QC, Canada) to induce a controllable and stable flowrate in the range of 1 to 14 μL/h. Pressure drop was measured through a pressure gauge sensor (MPS 1; Elveflow, Paris, France) connected to the inlet of the microfluidic chip. To record pressure data, the pressure sensor is connected to the flow reader (MSR OB1; Elveflow, Paris, France) which in turn transmits data to a computer. An inverted confocal microscope (Olympus FV-1000; Center Valley, PA) was used to monitor changes in RGC fluorescence intensity.

Agarose is a marine-based polysaccharide derivative of agar with desirable characteristics such as low gelling temperature, biocompatibility, and high mechanical strength.³¹ This gel is formed by a physical association of polysaccharide chains that become soluble in water at high temperatures. When the temperature is lowered, the agarose chains merge to construct double helical fibrils that form fibers and void space.³² Extensive efforts have been made to understand the transport phenomena and mechanical behavior of agarose such as stress relaxation behavior,³³ pore size measurements,^{34,35} fluid pressurization,³³ viscoelasticity,³⁶ and permeability varia-

tions.^{37,38} However, using agarose as a porous matrix to control the pressure increase in a microfluidic chamber has not been done. For any porous medium, the pressure drop is directly related to the hydraulic resistance and is governed by the permeability of the matrix. Johnson and Deen were the first to study the permeability of agarose with concentrations ranging from 2 to 7.3%.³⁷ Because of the low modulus and concentration of agarose, its permeability relies on the deformation of the porous domain when subject to a pressure drop. To study this, Gu et al. conducted comprehensive permeability measurements of agarose gels over a wide range of concentration (2–14.8%).³⁸ Their results suggest that the permeability is directly related to the void volume fraction (porosity) as well as the solidity and deformation of the gel under stress.³⁸

To test the response of retina to applied pressure, the excised retina was placed on a slice of agarose gel, which was cast in a 7 mm inner diameter glass tube. Once the tissue was flattened on the agarose, the cylinder was inverted and inserted into the open region of the PDMS Layer 1 (retina well, Figure 1c). The cylinder was then removed, leaving the agarose slab with the retina adhered to the glass coverslip. It was found that the agarose slab could prevent the retina from potential movement, allowing for a fixed position for imaging over the course of the experiment. Figure 1e shows a large field view of a mouse retina flat-mounted in the platform with the help of the agarose slab. The cholera toxin B (CTB) subunit conjugated to the fluorophore Alexa Fluor-488 was added to live retina, where it is actively taken up and transported along RGC axons.³⁹ The CTB serves as a tool to image retinal cells and their axons, which can be easily distinguished in Figure 1e. Importantly, the porous agarose gel allows media to perfuse through to keep the tissue healthy for the duration of the experiment. The microfluidic platform was then filled with culture media, and PDMS Layer 2 was bonded to PDMS Layer 1 via the adhesive tape to seal the platform. The inlet tubing was connected to the syringe pump to start the media flow. Lastly, after baseline imaging, the tube containing the solidified agarose was connected to the outlet tubing, allowing for pressure elevation in the chamber. Figure S2 shows a picture of the assembled device after a pressure experiment, where it is possible to see the retina and the agarose gel.

Animal Procurement and Ethics Statement. All animal studies were conducted in accordance with the National Institutes of Health (NIH) Guide for the Care and Use of Laboratory Animals and were approved by the IACUC committee at Vanderbilt University Medical Center. For this study, 12-week-old wild type Sv/129S6 mice were bred and housed at the Vanderbilt University Medical Center. Mice were maintained on a 12 h light/dark cycle with *ad libitum* access to standard mouse chow and water. All mice were euthanized with 10 mg intraperitoneal pentobarbital injection.

RESULTS AND DISCUSSION

Device Performance Characterization. To achieve and maintain targeted pressure levels, it is important to understand flow through the porous media. The total pressure drop is directly related to the total hydraulic resistance of the device, R_{total} , which is the sum of each component as follows.

$$R_{\text{total}} = R_t + R_c + R_p + R_{\text{minor}} \quad (1)$$

where R_t is the hydraulic resistance of tubing and fittings; R_c is the resistance of the rectangular channels; R_p is the resistance

developed by the porous matrix; and R_{minor} corresponds to other minor losses like bends, inlet, outlet, and interconnections. Each resistance is determined by the fluid properties, channel dimensions, surface roughness, and permeability.⁴⁰ In order to simplify the resistances and uncertainty of the measurements, R_t and R_c were first determined by measuring the pressure drop without the porous matrix, showing a pressure drop of 0.1 mmHg with a flowrate of 12 $\mu\text{L}/\text{h}$. As such, R_t and R_c are negligible with the flowrates used in this study. R_{minor} losses, as demonstrated by Akbari et al., are also negligible unless a higher Reynolds number (Re) is involved.⁴¹ Therefore, the component that dominates the pressure drop in this system is R_p .

Flow through porous media has been extensively studied, and different models have been derived. In the laminar flow regime with low Reynolds numbers, Darcy's law and Brinkman's equation are the most widely accepted models. These models represent variations of the momentum equation, which is the analog of the Navier–Stokes equation in the porous domain.²¹ Darcy's law describes a linear relationship between the flowrate and pressure drop as follows:

$$v_z = -\frac{K}{\mu} \frac{\partial P}{\partial z} \quad (2)$$

where v_z is the volume averaged velocity in the flow direction ($v_z = Q/A$, m/s), μ is the dynamic viscosity of the fluid (Pa·s), K is the Darcy permeability of the porous matrix (m^2), and $\partial P/\partial z$ is the pressure gradient in the flow direction ($\partial P/\partial z = \Delta P/L$, Pa/m) (Figure 2a). It should be noted that in the above

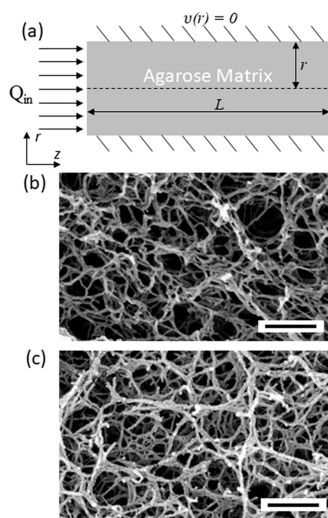


Figure 2. (a) Schematic of the flow through the agarose resistance matrix. Flow enters the porous domain from the left, filling the void space of the porous structure and raising the pressure drop. SEM image of critical point dried agarose at 1% (b) and 3% w/v (c). Pore sizes are larger in 1% agarose, which corresponds to a larger void volume or porosity. Scale bars are 200 nm.

equation, a no-slip boundary condition is assumed at the channel walls. This equation has been supported theoretically using both deterministic and statistical models,⁴² as well as experimentally,⁴³ and is widely accepted for Reynolds numbers of less than unity. As a result of the dense porous matrix and low flowrates used, the Reynolds number in our study is estimated to be on the order of 10^{-4} , allowing us to use the

Darcy's law to calculate the agarose permeabilities from pressure measurements.

R_p in eq 1 is largely influenced by the permeability, K , making it one of the most important parameters to study. Permeability measures the ability of a fluid to pass through a porous domain, which is directly related to the porosity, solidity, and deformation of the gel under stress. To achieve and maintain desired pressures with specified flowrates, we perform a thorough characterization of the gel permeability. To compare our measured agarose permeability with the reported values in the literature, the porosity (ϕ) of undeformed agarose must be derived first, which is expressed as follows:

$$\phi = 1 - \varepsilon = 1 - \frac{c}{\rho\omega} \quad (3)$$

where ε is the fiber volume fraction, c is the concentration of the gel (g/mL), ρ is the density of dry agarose (1.64 g/mL),⁴⁴ and ω is the mass fraction of agarose in a fiber, which is reported to be 0.625.⁴⁵ The porosity represents the amount of void space in the porous structure and is directly related to the concentration of agarose. Figure 2b, c shows scanning electron microscopy (SEM) images of the 1 and 3% agarose samples, respectively, prepared using a critical point dryer SAMDRI-PVT-3D (Tousimis; Rockville, Maryland). As shown in the SEM micrographs, the pore diameter is larger for the 1% sample, and the fiber diameter is larger for the 3% sample, making the porosity of the 1% agarose higher than that of the 3% agarose. This observation is consistent with eq 3.

In the permeability characterization, agarose gels of 1, 2, 3, and 3.75% concentrations were subject to continuous flow for extended periods of time. The applied flowrate was increased by steps after the pressure at each flowrate was stabilized for several hours without significant fluctuations. Figure 3a shows the raw pressure data for the 2% agarose in a flowrate range from 4 to 12 $\mu\text{L}/\text{h}$ with a step increase of 2 $\mu\text{L}/\text{h}$ every 24 h. The pressure is relatively stable over a long period of time, demonstrating the capability of the agarose to incrementally increase and maintain the pressure inside the chamber. Figure 3b plots measured pressure drop versus flowrate for different concentrations of agarose gels and indicates a linear relationship for all agarose concentrations. This linearity is attributed to the low Reynolds number involved with the flow governed by Darcy's law with minimal errors.

The permeability of agarose at different concentrations is derived from eq 2 after converting the flowrate to volume-averaged velocity, as depicted in Figure 3c as a function of flowrate. The gel porosity is directly related to its dilation,³⁸ and as the flowrate and pressure increase, the gel is subject to larger deformation by compressing the void space, leading to reduced permeability. Following the approach as reported by Johnson and Deen,³⁷ the permeability values of undeformed agarose (K_0) were determined by extrapolating to zero flowrate and plotted as a function of ϕ (Figure 3d). The permeabilities for 1% ($\phi = 0.9902$), 2% ($\phi = 0.9805$), 3% ($\phi = 0.9707$), and 3.75% ($\phi = 0.9634$) agarose are found to be 1569.6 ± 600.2 , 631.4 ± 45.5 , 200.8 ± 38.2 , and $102.1 \pm 22.1 \text{ nm}^2$, respectively. Overall, the undeformed permeability data obtained here are in good agreement with those reported by Gu et al.³⁸ extracted by dynamic loading. The results also align well with the empirical formula Gu et al. proposed, as described below:

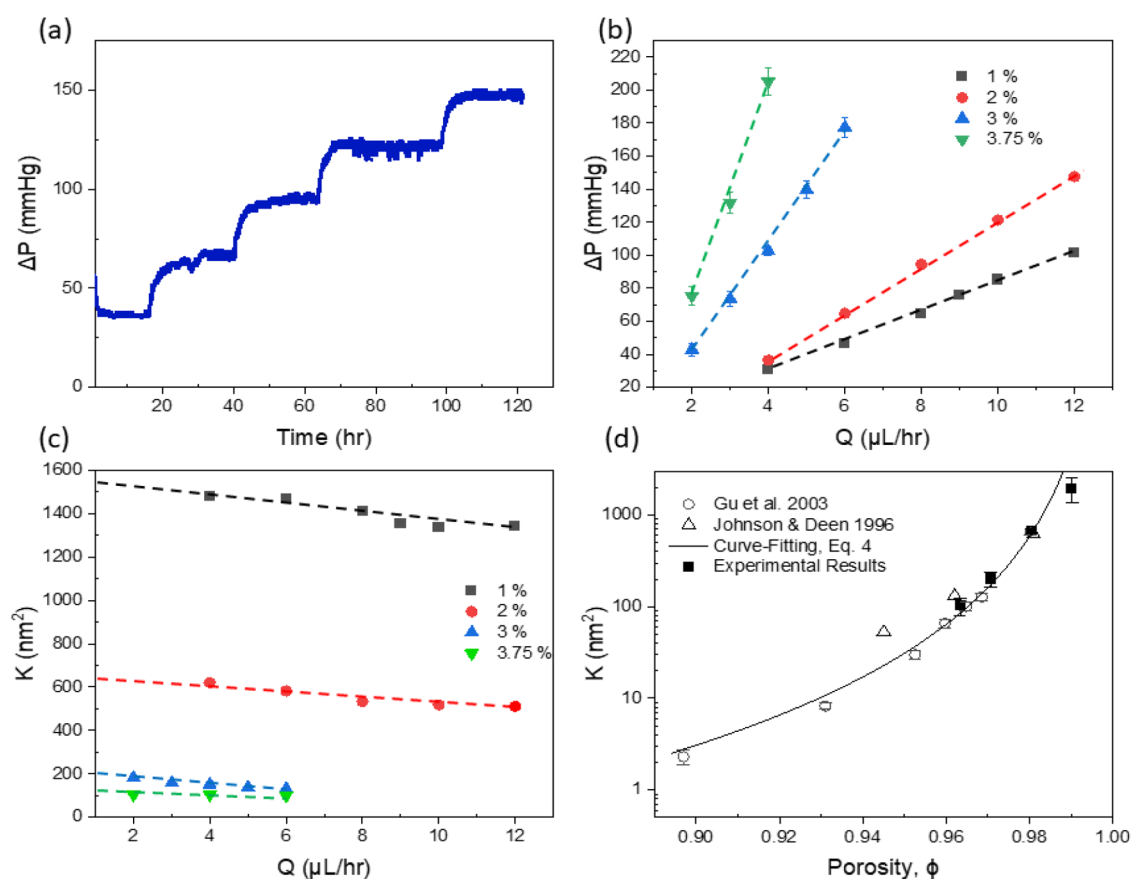


Figure 3. (a) Raw pressure data of 2% ($\phi = 0.9805$) agarose at five different applied flowrates ranging from 4 to 12 $\mu\text{L}/\text{h}$ with a 2 $\mu\text{L}/\text{h}$ step. (b) Chamber pressure drop vs flowrate for 1, 2, 3, and 3.75% agarose. Experimental data show a linear trend for the four concentrations. Error bars represent the mean \pm SD of 50,000+ data points for each flowrate. (c) Effect of applied flowrate (i.e., pressure) on the Darcy permeability measurements for four agarose concentrations. Trendlines were extrapolated to 0 $\mu\text{L}/\text{h}$ to obtain the undeformed agarose permeability in each case. (d) Extrapolated Darcy permeability of undeformed agarose as a function of its porosity. Data from Johnson and Deen³⁷ and Gu et al.³⁸ are plotted for comparison. Error bars represent the mean \pm SD for $n = 3$ sample size.

$$K = \alpha \left(\frac{\phi}{\epsilon} \right)^{3.236} \quad (4)$$

where $\alpha = 0.003399 \text{ nm}^2$. Table 1 summarizes the physical characteristics of the samples studied and their respective

Table 1. Undeformed Agarose Concentration, Porosity, Length, and Permeability

c [g/mL]	ϕ (eq 3)	L [cm] (eq 2)	K_0 [nm^2]
1%	0.9902	3.50	1569.6 ± 600.2
2%	0.9805	1.75	631.4 ± 45.5
3%	0.9707	1.20	200.8 ± 38.2
3.75%	0.9634	1.10	102.1 ± 22.1

permeability values. It should be noted that we adjusted the agarose length for different gel concentrations to allow for the ΔP vs Q curves to fit in a comparable ΔP range for plotting purpose.

Dynamic Response of Explanted Retina to Elevated Pressures. To demonstrate the imaging capability of our platform, we probed the response of explanted retina to elevated pressures by examining intracellular Ca^{2+} fluorescence of RGCs with the cell-permeable Ca^{2+} dye Fluo-4 AM.^{12,13} To quantify fluorescence intensity changes of RGCs over time, we calculated the mean fluorescence intensity change with respect

to the background of each image ($\Delta F/F_0$). Figure 4f depicts the RGC selection that the software FIJI performs on Figure 4e after threshold and size filtering. To ensure that the signal from Fluo-4 AM was stable under ambient pressure (in the device without pressure initiated), we monitored Fluo-4 activity of RGCs over a period of 2 h (representative trace in Figure 4a). Fluorescent signal remained stable, with only a minor nonsignificant fluctuation between $t = 0$ and $t = 120$ min (Figure 4a; representative image of RGC fluorescence shown in Figure 4c; $t = 0$ min, $\Delta F/F_0 = 3.02 \pm 0.36$ A.U. vs $t = 120$ min, $\Delta F/F_0 = 3.67 \pm 0.63$ A.U., Welch's T -test).

In the pressurized test, measurements were first taken in the device at ambient pressure for 20 min and were considered a baseline. During pressurized test 1, the fluorescent signal at the baseline displayed a mean $\Delta F/F_0$ of 3.99 ± 0.42 A.U., comparable to the reading from the control experiment of 3.21 ± 0.45 A.U. (Figure 4b, representative RGC image shown in Figure 4d). These baseline recordings were stable and similar to the control experiment in tests 2 and 3 (Figure S3). The chamber pressure was then rapidly increased to 87.68 ± 7.63 mmHg (Figure 4a; black line graph). The overshoot in pressure at the 20 min timepoint is most likely due to the alteration of the agarose gel structure upon elevated pressure.⁴⁶ For the three pressure tests, the peak value was on average 32.2% larger than the pressure after 100 min. In response to the elevated chamber pressure, RGCs displayed, on average, an

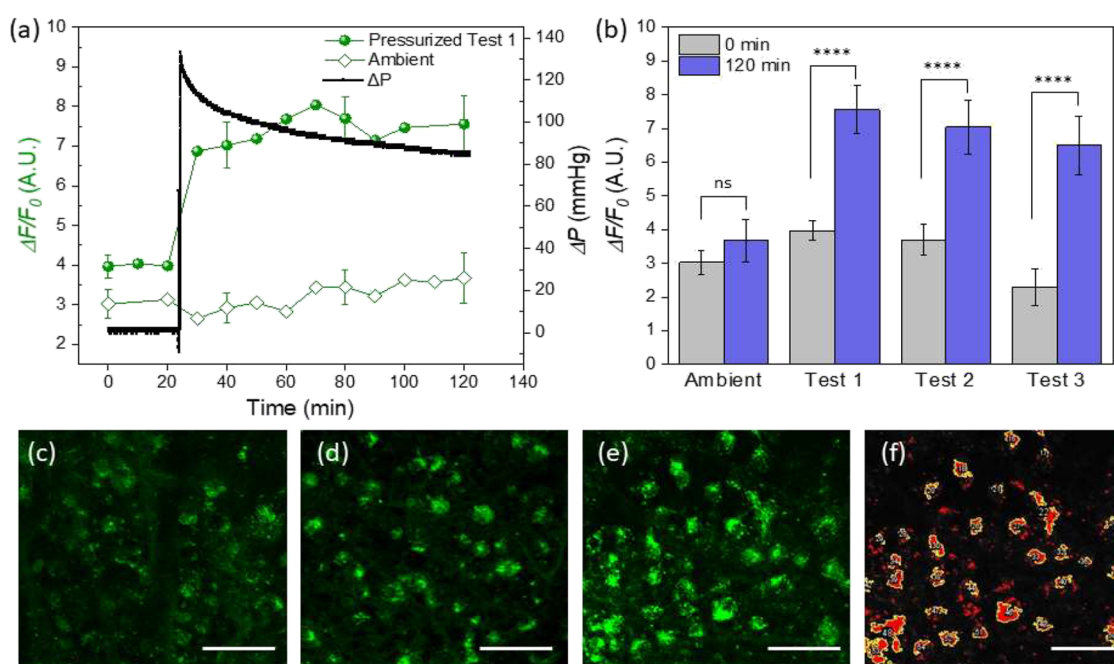


Figure 4. (a) Representative trace showing $\Delta F/F_0$ of ambient and elevated pressure studies of RGCs with Ca^{2+} intracellular dye Fluo-4 AM. Ca^{2+} fluorescence increase is directly related to pressure increase. (b) Cells maintained at ambient pressure showed no significant change in fluorescence. Exposure to elevated pressure significantly increases the intracellular calcium flux in RGCs, reflected by an average 119.16% change in fluorescence with pressure. (c) Fluo-4 AM conjugated Ca^{2+} accumulation in whole retinal RGCs exposed for 120 min ambient pressure. (d) Fluo-4 AM conjugated Ca^{2+} accumulation in whole retinal RGCs at baseline without pressure. (e) Fluo-4 AM conjugated Ca^{2+} accumulation in whole retinal RGCs exposed for 120 min elevated pressure. (f) Visual representation of Figure 4e where selected ROIs are visible after applying thresholding and size filtering. Fluorescent intensity of each pixel is then measured for each cell. 30+ cells were measured per analysis. Scale bars are 50 μm . Data shown as mean \pm SEM.

immediate and significant 119.16% increase in fluorescence due to calcium influx, similar to the increase observed in primary RGC cultures¹⁵ (representative trace shown in Figure 4a, additional traces shown in Figure S3). Test 1 demonstrated an 85.46% increase ($****p < 0.0001$, $t = 0$ min, $\Delta F/F_0 = 3.96 \pm 0.28$ A.U. vs $t = 120$ min, $\Delta F/F_0 = 7.56 \pm 0.71$ A.U., Welch's *T*-test). Pressurized tests 2 and 3 show a 90.16 and 181.85% increase, respectively (Figure 4b; Test 2 $****p < 0.0001$; $t = 0$ min, $\Delta F/F_0 = 3.70 \pm 0.46$ A.U. vs $t = 120$ min, $\Delta F/F_0 = 7.04 \pm 0.79$ A.U., Welch's *T*-test; and Test 3; $****p < 0.0001$; $t = 0$ min, $\Delta F/F_0 = 2.30 \pm 0.54$ A.U. vs $t = 120$ min, $\Delta F/F_0 = 6.49 \pm 0.87$ A.U., Welch's *T*-test). The tests show a consistent trend of elevation in Ca^{2+} due to increased pressure; the range in data is most likely due to biological variations across samples. Finally, we tested a dynamic change in pressure within a closed experiment. Retina was exposed to an elevated pressure for 40 min and then reduced pressure to the baseline (Figure S4a). Interestingly, after the elevated pressure was removed, Ca^{2+} fluorescence remained stable for a further 30 min, before decreasing slowly by 30% at 120 min ($****p < 0.0001$; $t = 0$ min, $\Delta F/F_0 = 2.52 \pm 0.25$ A.U. vs $t = 60$ min, $\Delta F/F_0 = 5.15 \pm 0.22$ A.U. vs 120 min, $\Delta F/F_0 = 4.34 \pm 0.35$ A.U., Welch's *T*-test).

We note that Ca^{2+} levels are maintained within neurons at relatively low and strongly controlled concentrations as Ca^{2+} can act on multiple cell signaling pathways.⁴⁷ Overactivation of Ca^{2+} signaling pathways caused by high-level influx of Ca^{2+} is harmful to neurons as it facilitates flux through the final common pathway for neuronal death in a variety of pathological conditions.¹¹ Our results in whole retina show a relative increase in Ca^{2+} almost immediately with pressure to

levels much higher than those observed during baseline measurements. Similar relative increases in Ca^{2+} fluorescence were observed in in vitro RGC experiments, which resulted in a significant 35% decrease in cell viability.¹⁵ Despite returning pressure to the baseline, our results indicate that Ca^{2+} fluorescence persists at elevated levels of 70–100% higher than the baseline. It is plausible that persistent elevation in Ca^{2+} without recovery to the baseline level would render cells more susceptible to death; however, more studies are required to explore this hypothesis. Dramatic pressure-induced changes in intracellular Ca^{2+} levels have been shown to trigger RGC death possibly through the activation of TRPV1 channels.¹⁵ However, further investigations into short-term Ca^{2+} increases in whole retinal tissue due to pressure and the effect on neurodegenerative pathways are warranted.¹¹ Our results report relative changes in calcium fluorescence using Fluo-4 AM.^{12,13} Such measurements are intended to provide relative changes in intracellular Ca^{2+} and are not indicative of absolute concentrations. Fluorescence intensity can be converted to absolute Ca^{2+} concentration after calibration of the dye in single-cell dye loading experiments.⁴⁸

CONCLUSIONS

In summary, we have developed a microfluidic chamber capable of imposing a wide range of operating pressures to examine the dynamic response of cells and tissues. Pressure can be elevated in a controlled manner by forcing flow through an agarose porous matrix. One advantage of the microfluidic device characterized in this study is that it provides a platform to measure a wide range of pressures in tissue and culture, with the possibility of not only measuring cell responses to acute,

stable pressure elevations but also to fluctuations in pressure. Furthermore, we confirm that live fluorescence imaging can be carried out in conjunction with changes in pressure through measuring the relative changes in intracellular RGC Ca^{2+} in response to elevated pressure. This overcame a previous limitation that intracellular Ca^{2+} cannot be measured at short time intervals in response to pressure elevation. We expect that this microfluidic platform will enable novel assays to probe the dynamic response of cells and tissues to pressure changes in a wide variety of ex vivo and in vitro settings.

■ ASSOCIATED CONTENT

SI Supporting Information

The Supporting Information is available free of charge at <https://pubs.acs.org/doi/10.1021/acs.analchem.1c05652>.

Fabrication details of SU-8 master mold via photolithography; PDMS slabs following soft-lithography techniques and PDMS–PDMS bonding; ex vivo retinal preparation and Ca^{2+} dye Fluo-4 AM loading to measure intracellular changes in fluorescence intensity; fluorescence imaging and postanalysis with FIJI software; and uncertainty analysis of agarose measurements and permeability calculations (PDF)

■ AUTHOR INFORMATION

Corresponding Authors

Lauren K. Wareham – Vanderbilt Eye Institute, Vanderbilt Medical Center, Nashville, Tennessee 37232, United States; Email: lauren.wareham@vumc.org

Deyu Li – Department of Mechanical Engineering, Vanderbilt University, Nashville, Tennessee 37235, United States; orcid.org/0000-0001-8364-0924; Email: deyu.li@vanderbilt.edu

Authors

Alberto Esteban-Linares – Department of Mechanical Engineering, Vanderbilt University, Nashville, Tennessee 37235, United States; orcid.org/0000-0002-8637-2977

Thayer S. Walmsley – Department of Physics and Astronomy, Vanderbilt University, Nashville, Tennessee 37235, United States

Joseph M. Holden – Vanderbilt Eye Institute, Vanderbilt Medical Center, Nashville, Tennessee 37232, United States

Matthew L. Fitzgerald – Department of Mechanical Engineering, Vanderbilt University, Nashville, Tennessee 37235, United States; orcid.org/0000-0002-9103-2328

Zhiliang Pan – Department of Mechanical Engineering, Vanderbilt University, Nashville, Tennessee 37235, United States; orcid.org/0000-0002-6154-2765

[†]Ya-Qiong Xu – Department of Electrical and Computer Engineering and Department of Physics and Astronomy, Vanderbilt University, Nashville, Tennessee 37235, United States; orcid.org/0000-0003-1423-7458

Complete contact information is available at: <https://pubs.acs.org/doi/10.1021/acs.analchem.1c05652>

Notes

The authors declare no competing financial interest.
[†]Y.-Q.X. is deceased.

■ ACKNOWLEDGMENTS

The work carried out in this manuscript was supported by the National Institutes of Health (1R01EY027729) and unrestricted departmental award and a Glaucoma Research Foundation Schaffer prize awarded to L.K.W. Images were obtained with the aid of Evan Krystofiak from the CISR (Cell Imaging Shared Resource) at Vanderbilt University Medical Center core facility. The authors thank Dr. Rebecca Sappington for helpful discussions.

■ REFERENCES

- (1) Pethő, Z.; Najder, K.; Bulk, E.; Schwab, A. *Cell Calcium* **2019**, *80*, 79–90.
- (2) Treichel, A. J.; Farrugia, G.; Beyder, A. *Brain Res.* **2018**, *1693*, 197–200.
- (3) Momin, A.; Bahrapour, S.; Min, H.-K.; Chen, X.; Wang, X.; Sun, Y.; Huang, X. *Trends Pharmacol. Sci.* **2021**, *42*, 367–384.
- (4) Bernardo-Colón, A.; Vest, V.; Cooper, M. L.; Naguib, S. A.; Calkins, D. J.; Rex, T. S. *Front. Neurosci.* **2019**, *13*, 719.
- (5) Bojikian, K. D.; Stein, A. L.; Slabaugh, M. A.; Chen, P. P. *Eye* **2015**, *29*, 1579–1584.
- (6) Leung, D. Y.-L.; Lam, D. S.-C. *Ann. Emerg. Med.* **2005**, *45*, 98–99.
- (7) Mohseni, M.; Blair, K.; Bragg, B. N. Blunt Eye Trauma. In *StatPearls*; StatPearls Publishing: Treasure Island (FL), 2021.
- (8) Calkins, D. J. *Prog. Retin. Eye Res.* **2021**, *84*, No. 100953.
- (9) Duncan, R. S.; Goad, D. L.; Grillo, M. A.; Kaja, S.; Payne, A. J.; Koulen, P. *Molecules* **2010**, *15*, 1168–1195.
- (10) Ali, F.; Kwan, A. C. *Neurophotonics* **2020**, *7*, No. 011402.
- (11) Prilloff, S.; Noblejas, M. I.; Chedhomme, V.; Sabel, B. A. *Eur. J. Neurosci.* **2007**, *25*, 3339–3346.
- (12) Sappington, R. M.; Calkins, D. J. *Invest. Ophthalmol. Vis. Sci.* **2008**, *49*, 3004–3017.
- (13) Gee, K. R.; Brown, K. A.; Chen, W.-N. U.; Bishop-Stewart, J.; Gray, D.; Johnson, I. *Cell Calcium* **2000**, *27*, 97–106.
- (14) Sappington, R. M.; Chan, M.; Calkins, D. J. *Invest. Ophthalmol. Vis. Sci.* **2006**, *47*, 2932–2942.
- (15) Sappington, R. M.; Sidorova, T.; Long, D. J.; Calkins, D. J. *Invest. Ophthalmol. Vis. Sci.* **2009**, *50*, 717–728.
- (16) Wu, J.; Mak, H. K.; Chan, Y. K.; Lin, C.; Kong, C.; Leung, C. K. S.; Shum, H. C. *Sci. Rep.* **2019**, *9*, 9057.
- (17) Ji, J.; Chang, P.; Pennesi, M. E.; Yang, Z.; Zhang, J.; Li, D.; Wu, S. M.; Gross, R. L. *Vision Res.* **2005**, *45*, 169–179.
- (18) Moleiro, A. F.; Conceição, G.; Leite-Moreira, A. F.; Rocha-Sousa, A. J. *Ophthalmol.* **2017**, *2017*, No. 3034953.
- (19) Ishikawa, M.; Yoshitomi, T.; Zorumski, C. F.; Izumi, Y. *Invest. Ophthalmol. Vis. Sci.* **2010**, *51*, 6414–6423.
- (20) Ishikawa, M.; Yoshitomi, T.; Covey, D. F.; Zorumski, C. F.; Izumi, Y. *Neuropharmacology* **2016**, *111*, 142–159.
- (21) Nield, D. A.; Bejan, A. *Convection in Porous Media*, 4th ed.; Springer-Verlag: New York, 2013.
- (22) Sampath, M.; Shukla, A.; Rathore, A. S. *Bioengineering* **2014**, *1*, 260–277.
- (23) Kim, J.; O'Hare, D. *Nano Converg.* **2018**, *5*, 19.
- (24) Galindo-Rosales, F. J.; Campo-Deaño, L.; Pinho, F. T.; van Bokhorst, E.; Hamersma, P. J.; Oliveira, M. S. N.; Alves, M. A. *Microfluid. Nanofluid.* **2012**, *12*, 485–498.
- (25) Gunda, N. S. K.; Joseph, J.; Tamayol, A.; Akbari, M.; Mitra, S. K. *Microfluid. Nanofluid.* **2013**, *14*, 711–721.
- (26) Throckmorton, D. J.; Shepodd, T. J.; Singh, A. K. *Anal. Chem.* **2002**, *74*, 784–789.
- (27) Yeom, J.; Agonafer, D. D.; Han, J.-H.; Shannon, M. A. J. *Micromech. Microeng.* **2009**, *19*, No. 065025.
- (28) Abdhussain, N.; Nawada, S.; Currihan, S.; Passamonti, M.; Schoenmakers, P. J. *Chromatogr. A* **2020**, *1623*, No. 461159.

- (29) Kocaoglu, O. P.; Uhlhorn, S. R.; Celdran, M.; Hernandez, E.; Porciatti, V.; Parel, J.-M.; Manns, F. *Invest. Ophthalmol. Vis. Sci.* **2007**, *48*, 1198.
- (30) Kratz, S. R. A.; Eilenberger, C.; Schuller, P.; Bachmann, B.; Spitz, S.; Ertl, P.; Rothbauer, M. *Sci. Rep.* **2019**, *9*, 9287.
- (31) Zarrintaj, P.; Manouchehri, S.; Ahmadi, Z.; Saeb, M. R.; Urbanska, A. M.; Kaplan, D. L.; Mozafari, M. *Carbohydr. Polym.* **2018**, *187*, 66–84.
- (32) Arnott, S.; Fulmer, A.; Scott, W. E.; Dea, I. C. M.; Moorhouse, R.; Rees, D. A. *J. Mol. Biol.* **1974**, *90*, 269–284.
- (33) Mauck, R. L.; Soltz, M. A.; Wang, C. C.; Wong, D. D.; Chao, P. H.; Valhmu, W. B.; Hung, C. T.; Ateshian, G. A. *J. Biomech. Eng.* **2000**, *122*, 252–260.
- (34) Narayanan, J.; Xiong, J.-Y.; Liu, X.-Y. *J. Phys. Conf. Ser.* **2006**, *28*, 83–86.
- (35) Pernodet, N.; Maaloum, M.; Tinland, B. *Electrophoresis* **1997**, *18*, 55–58.
- (36) Ahearne, M.; Yang, Y.; El Haj, A. J.; Then, K. Y.; Liu, K.-K. *J. R. Soc., Interface* **2005**, *2*, 455–463.
- (37) Johnson, E. M.; Deen, W. M. *AIChE J.* **1996**, *42*, 1220–1224.
- (38) Gu, W. Y.; Yao, H.; Huang, C. Y.; Cheung, H. S. *J. Biomech.* **2003**, *36*, 593–598.
- (39) Angelucci, A.; Clascá, F.; Sur, M. *J. Neurosci. Methods* **1996**, *65*, 101–112.
- (40) Choi, S.; Lee, M. G.; Park, J.-K. *Biomicrofluidics* **2010**, *4*, No. 034110.
- (41) Akbari, M.; Sinton, D.; Bahrami, M. *J. Fluids Eng.* **2009**, *131*, No. 041202.
- (42) Whitaker, S. *Transp. Porous Media* **1986**, *1*, 3–25.
- (43) Alabi, O. Validity of Darcy's Law in Laminar Regime. *Electron. J. Geotech. Eng.* **2011**, *16*.
- (44) Laurent, T. C. *Biochim. Biophys. Acta, Gen. Subj.* **1967**, *136*, 199–205.
- (45) Johnson, E. M.; Berk, D. A.; Jain, R. K.; Deen, W. M. *Biophys. J.* **1995**, *68*, 1561–1568.
- (46) Esteki, M. H.; Alemrajabi, A. A.; Hall, C. M.; Sheridan, G. K.; Azadi, M.; Moeendarbary, E. *Acta Biomater.* **2020**, *102*, 138–148.
- (47) Rasmussen, H. *Sci. Am.* **1989**, *261*, 66–73.
- (48) Berna-Erro, A.; Braun, A.; Kraft, R.; Kleinschnitz, C.; Schuhmann, M. K.; Stegner, D.; Wultsch, T.; Eilers, J.; Meuth, S. G.; Stoll, G.; Nieswandt, B. *Sci. Signaling* **2009**, *2*, ra67.

Recommended by ACS

Microfluidic Platform to Transduce Cell Viability to Distinct Flow Pathways for High-Accuracy Sensing

Fatima Ezahra Chrit, Todd Sulchek, *et al.*

SEPTEMBER 21, 2021
ACS SENSORS

READ 

Microengineered Flexural Post Rings for Effective Blood Sample Fencing and High-Throughput Measurement of Clot Retraction Force

Lanzhu Huang, Zida Li, *et al.*

NOVEMBER 16, 2020
ACS SENSORS

READ 

Automated Cell Mechanical Characterization by On-Chip Sequential Squeezing: From Static to Dynamic

Pengyun Li, Tatsuo Arai, *et al.*

JUNE 25, 2021
LANGMUIR

READ 

Integrated Acoustic Chip for Culturing 3D Cell Arrays

Yong Luo, Xueji Zhang, *et al.*

SEPTEMBER 01, 2022
ACS SENSORS

READ 

Get More Suggestions >